THE JOURNAL OF PHYSICAL CHEMISTRY C
A JOURNAL OF THE AMERICAN CHEMICAL SOCIETY

pubs.acs.org/JPCC
Article

Bismuth-Based Perovskite Derivates with Thermal Voltage Exceeding 40 mV/K

Vanira Trifiletti,* Matteo Massetti, Alberto Calloni, Sally Luong, Andrea Pianetti, Silvia Milita, Bob C. Schroeder, Gianlorenzo Bussetti, Simona Binetti, Simone Fabiano, and Oliver Fenwick*

Cite This: J. Phys. Chem. C 2024, 128, 5408−5417

ABSTRACT: Heat is an inexhaustible source of energy, and it can be exploited by thermoelectronics to produce electrical power or electrical responses. The search for a low-cost thermoelectric material that could achieve high efficiencies and can also be straightforwardly scalable has turned significant attention to the halide perovskite family. Here, we report the thermal voltage response of bismuth-based perovskite derivates and suggest a path to increase the electrical conductivity by applying chalcogenide doping. The films were produced by drop-casting or spin coating, and sulfur was introduced in the precursor solution using bismuth triethylxanthate. The physical−chemical analysis confirms the substitution. The sulfur introduction caused resistivity reduction by 2 orders of magnitude, and the thermal voltage exceeded 40 mV K^{-1} near 300 K in doped and undoped bismuth-based perovskite derivates. X-ray diffraction, Raman spectroscopy, and grazing-incidence wide-angle X-ray scattering were employed to confirm the structure. X-ray photoelectron spectroscopy, elemental analysis, scanning electron microscopy, and energy-dispersive X-ray spectroscopy were employed to study the composition and morphology of the produced thin films. UV−visible absorbance, photoluminescence, inverse photoemission, and ultraviolet photoelectron spectroscopies have been used to investigate the energy band gap.

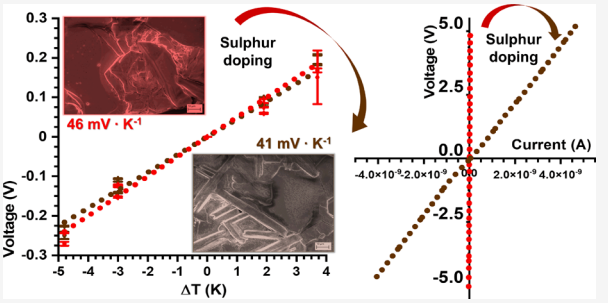

1. INTRODUCTION

Halide perovskites can be assembled into bulk materials containing low-dimensional units.[1] The term perovskite is reserved for materials with an ABX_3 stoichiometry consisting of a three-dimensional arrangement of connected metal halide octahedra, while, here, we will refer to compounds containing A cations, B metals, and X halides that deviate from this structure as halide perovskite derivates, such as the Bi-based compounds.[2−5] When they are set in the $A_3Bi_2X_9$ configuration, they are typically arranged in two- and zero-dimensional structures. In vacancy-ordered derivates (e.g., $Rb_3Bi_2I_9$ and $K_3Bi_2I_9$), bismuth cations occupy 2/3 of the B sites, so the vacancies are aligned along a single plane, forming a two-dimensional layer of bismuth iodide octahedra. On the other hand, when monovalent cations, such as Cs^+, $CH(NH_2)^{2+}$, or $CH_3NH_3^+$, occupy the A site, the elements are placed in a zero-dimensional hexagonal structure, isolating the $[Bi_2I_9]^{3-}$ dimers.[1,4,5] Low-dimensional perovskite derivates are increasingly attracting the interest of applied research, first of all for their chemical stability and low toxicity[6,7] and then because the phenomena resulting from charge confinement open new frontiers for technologies such as photovoltaics, photodetectors, LEDs, lasing, capacitors, memristors, thermoelectrics, and sensors.[4,5]

For instance, much of the energy we produce as a society ends up as high- or low-grade waste heat, which could be recovered since a temperature difference can create electrical power by exploiting the physical phenomenon called thermoelectricity.[8] The thermoelectric conversion efficiency is related to the figure of merit $zT = (S^2\ \sigma)T/k$ of the thermoelectric material used (wherein T is the temperature, k and σ are the thermal and electrical conductivity, respectively, and S is the Seebeck coefficient).[9] Therefore, materials with low thermal conductivity and high Seebeck coefficient, or high thermal voltage, are good candidates for efficient thermoelectric applications.[10−13] Halide perovskites have already been proven to have ultralow thermal conductivity and good Seebeck coefficients, but they have a low zT due to their high electrical resistivity.[1,11,13−16] However, research in the field is accelerating thanks to computational predictions of zT exceeding 1 (even up to 2.6 at suitable doping concentrations),[17−19] to the experimental demonstrations of zT > 0.1,[15,20,21] to their

Received: September 21, 2023
Revised: March 1, 2024
Accepted: March 4, 2024
Published: March 26, 2024

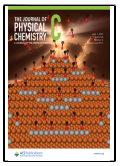

https://doi.org/10.1021/acs.jpcc.3c06324
J. Phys. Chem. C 2024, 128, 5408−5417

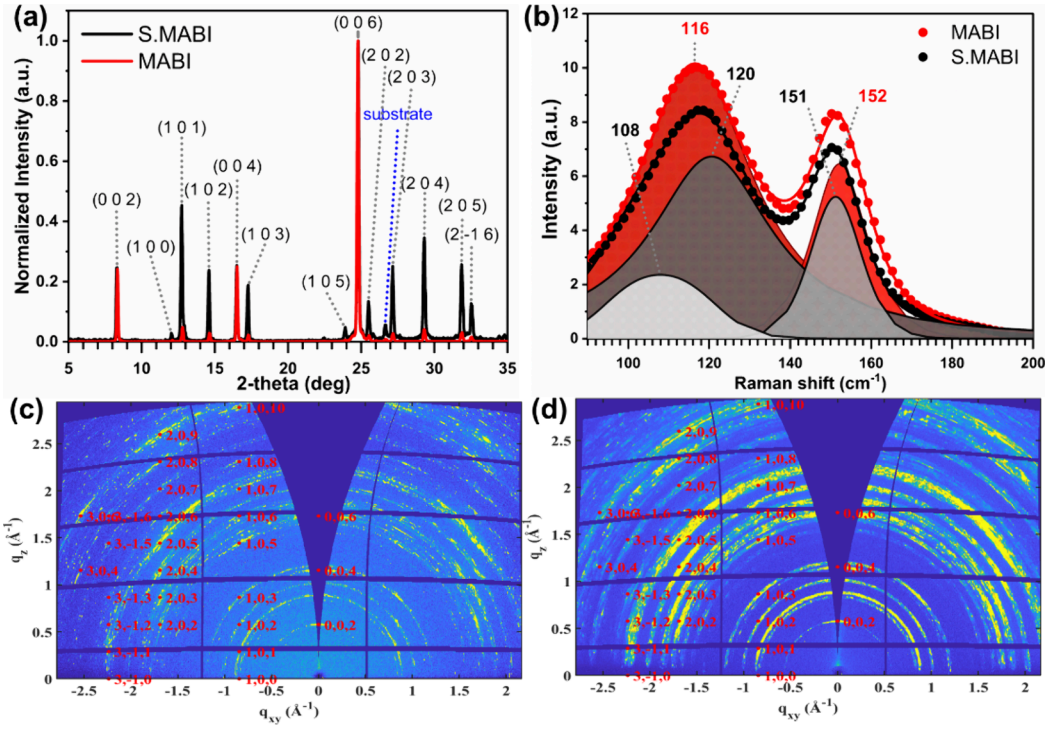

Figure 1. (a) XRD and (b) Raman spectra of sulfur-doped, S.MABiI, and undoped MABiI layers (raw data in Raman depicted as dots, fitting with straight lines and deconvoluted peaks by curves with the filled area) produced by drop-casting (to have thick samples, so defined diffractions with high intensity) on FTO-coated glass; grazing incidence wide-angle X-ray scattering (GIWAXS) patterns of (c) MABiI and (d) S.MABiI thin film deposited by spin coating (to have flat samples, so defined diffractions not influenced by the surface morphology) on FTO-coated glass.

straightforward processability, and to the tunable composition. Moreover, it is known that top-down material nanostructuring can be used to reduce the thermal conductivity through increased phonon scattering at the grain boundaries and increase the Seebeck coefficient since it is determined by the sharpness of the density of states near the Fermi level (it is maximized when the energy levels are discrete).[10,22] The thermal conductivity of halide perovskites can be reduced as the dimensionality decreases and as the stoichiometry deviates from ABX_3: thermal conductivity of 0.53 W m^{-1} K^{-1} was measured in the 3D phase of $CsPbCl_3$, 0.40 W m^{-1} K^{-1} in 2D $CsPb_2Cl_5$, and 0.30 W m^{-1} K^{-1} in 0D Cs_4PbCl_6.[23] An even lower value, 0.23 W m^{-1} K^{-1}, has been reported in $(CH_3NH_3)_3Bi_2I_9$ (MABiI), a quasi-0D perovskite belonging to the vacancy ordered family.[24] Long et al. registered a thermal voltage of 2.6 mV K^{-1} and thermal conductivity of 0.21 W m^{-1} K^{-1} in MABiI pellets.[11] However, the resistivities reported until today in most halide perovskite and derivative systems are too high to reach the predicted zT. As extrinsic doping can enhance the electrical conductivity in the 3D halide perovskite,[16] bismuth triethylxanthate, $Bi(xt)_3$, has been used as an effective dopant for MABiI,[11,25,26] partially substituting Bi with S. Authors reported carrier mobility of 2.3 cm^2 V^{-1} s^{-1} and carrier concentrations of about 10^{21} cm^{-3} in sulfur-doped $(CH_3NH_3)_3Bi_2I_9$ (S.MABiI) thin films.[25]

In this context, we studied the thermal voltage in bismuth-based perovskite-derivative thin films, and the beneficial halide substitution with chalcogens has been proven and explained. Since the thermal voltages generated in our films are so large, they cannot be purely attributed to a Seebeck effect. Despite scaling with the temperature difference in the same way as a Seebeck voltage, the more general term of "thermal voltage" is used in this report since its origin is likely different. MABiI was studied by producing thin films by drop-casting or spin coating, and the halide substitution with sulfur has been demonstrated. The thermovoltage registered was remarkable as well as the decrease in resistivity gained upon sulfur substitution. The impact on the optoelectronic properties and the charge confinement has been clarified, and a model suggested.

2. RESULTS AND DISCUSSION

The crystal structure of S.MABiI and MABiI films, produced by drop-casting, showed hexagonal symmetry belonging to the $P6_3/mmc$ space group, as confirmed by XRD (Figure 1a).[25,27−31] The main diffraction plain is (006) in both samples. In MABiI, the (00l) planes dominate the XRD spectrum, while (h0l) peaks are also significant in S.MABiI, indicating a less oriented polycrystalline structure than the undoped compound. Raman spectroscopy (Figure 1b) confirms that the $[Bi_2I_9]^{3-}$ octahedra are bonded to the $CH_3NH_3^+$ cations.[7,26,31] The peak at 116 cm^{-1} in the MABiI spectrum shifts to 120 cm^{-1} in S.MABiI, where a peak arises at 108 cm^{-1}. This has previously been reported in sulfur-doped MABiI samples,[26] and it is related to the sulfur inclusion in the structure. To confirm the crystalline structures and texturing of the films, grazing incidence wide-angle X-ray scattering (GIWAXS) was performed on films prepared by spin coating, which are suitable to be studied with this technique due to their low roughness. Figure 1c shows the MABiI 2D images: the positions of the diffraction signals fit, within the experimental errors, those corresponding to the bulk hexagonal phase (space group $P6_3/mmc$).[32] Furthermore, the intensity distribution along the Debye rings allows us to establish that the film consists of randomly distributed crystallites with c axis preferentially oriented perpendicular to the substrate but

https://doi.org/10.1021/acs.jpcc.3c06324
J. Phys. Chem. C 2024, 128, 5408−5417

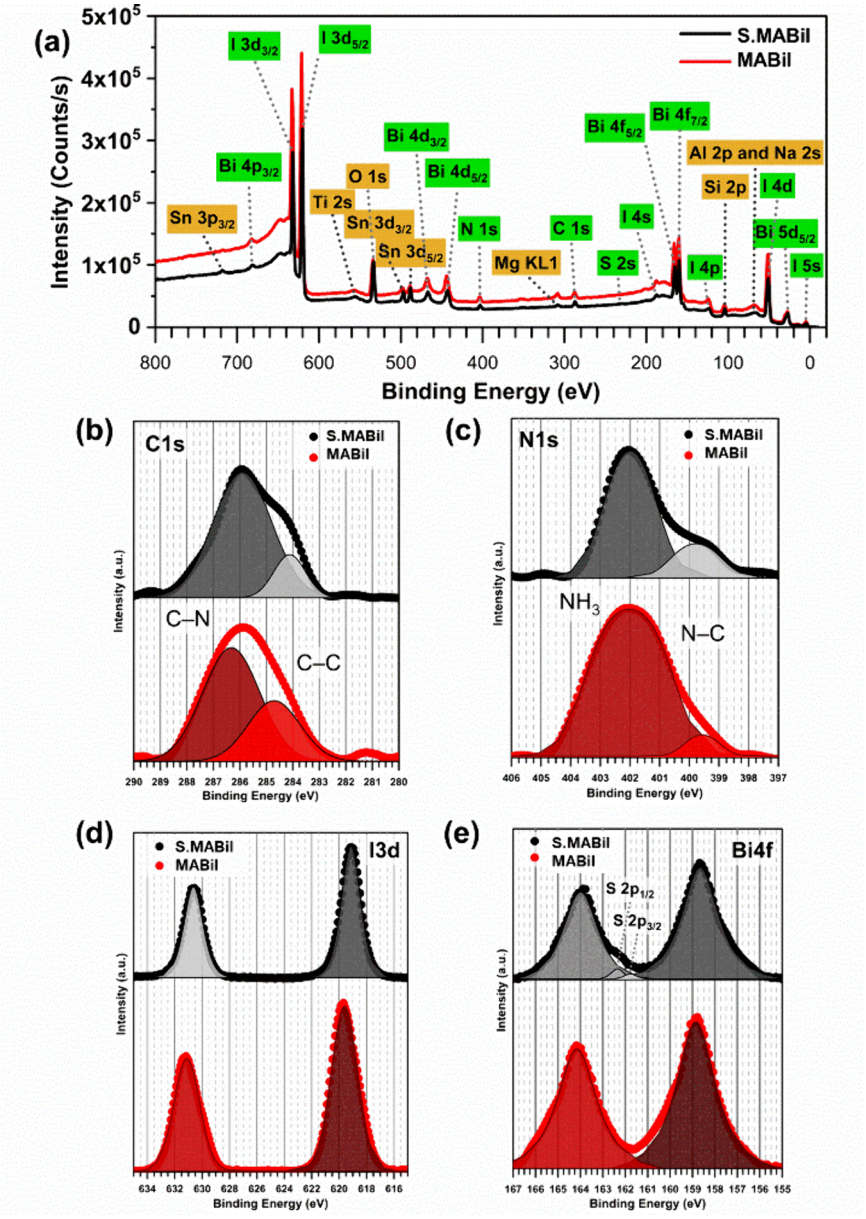

Figure 2. (a) XPS survey spectra of the sulfur-doped S.MABiI and undoped MABiI films produced by drop-casting in a nitrogen-filled glovebox on soda-lime glass. XPS high-resolution core-level spectra, related to sulfur-doped S.MABiI and undoped MABiI layers produced by drop-casting in a nitrogen-filled glovebox on soda-lime glass for (b) C 1s, (c) N 1s, (d) I 3d, and (e) Bi 4f (Raw data depicted as dots, fitting with straight lines and deconvoluted peaks by curves with the filled area).

randomly oriented in the plane of the substrate (symmetric distribution around the vertical direction, q_z). Similarly, a 2D-GIWAXS image is presented for S.MABiI confirming the space group $P6_3/mmc$. Therefore, the structural analysis indicates that the iodine substitution with sulfur strains the structure within the tolerance factor of the $P6_3/mmc$ space group. A representation of the crystalline structure of MABiI is reported in Figure S1, showing the unit cell in all three directions, along the c axis, and a supercell $2 \times 2 \times 2$.

Analysis of XPS spectra helped confirm the elemental composition. Peaks corresponding to C, N, Bi, I, and S can be identified in the XPS survey spectra of S.MABiI and MABiI (Figure 2a). Multiple other elements can be ascribed to the soda-lime glass substrate (labeled in orange in Figure 2a): the large sampling area (1 mm diameter), pinholes in the film, and ion beam etching explain the substrate's significant contribution. High-resolution core-level C, N, I, and Bi spectra are presented in Figure 2b–e. The C 1s spectrum (Figure 2b) shows the expected two components, one from the C–C bond at 284.5 eV and the other from the C–N at 286 eV. The N 1s spectrum (Figure 2c) is deconvoluted into two spectral contributions: the single-bonded nitrogen with carbon atoms (N–C) around 400 eV, and the peak at 402 eV attributed to the amide group $-NH_3^+$ in $CH_3NH_3^+$.[7,33−36] I $3d_{3/2}$ at 631 eV and I $3d_{5/2}$ at 619 eV (Figure 2d) are attributed to I^-. Bi 4f and S 2p peaks overlap, but a small S 2p signal at ∼162 eV on the larger Bi 4f peak in the S.MABiI sample can be ascribed to the sulfur contribution. Figure 2e displays the spectral deconvolution and the raw data: Bi $4f_{5/2}$ is set at 164 eV and Bi $4f_{7/2}$, at 159 eV, indicating that bismuth is in the Bi^{3+} state, following the reported literature.[7,25,35,37] In the S.MABiI Bi 4f spectrum (Figure 2e), the two spectral contributions from $2p_{3/2}$ and S

https://doi.org/10.1021/acs.jpcc.3c06324
J. Phys. Chem. C 2024, 128, 5408−5417

Table 1. Calculated Mass Fraction of C, H, N, and S in MABiI and S.MABiI in $(CH_3NH_3)_3I_{9-x}S_x$

sample	C (wt %)	H (wt %)	N (wt %)	S (wt %)	molecular formula, $(CH_3NH_3)_3I_{9-x}S_x$
MABiI	2.94	1.16	2.69	0.00	$(CH_3NH_3)_3Bi_2I_9$
S.MABiI	2.81	1.15	2.48	0.61	$(CH_3NH_3)_3Bi_2I_{8.9}S_{0.1}$

$2p_{1/2}$ can be identified at 161.8 and 162.3 eV,[26] confirming sulfur inclusion in the structure. A slight I 3d and Bi 4f peak shift to lower energy is registered in S.MABiI compared to the undoped samples. This could be ascribed to the sulfur inclusion in the structure. Sulfur contents in S.MABiI have been revealed by CHNS elemental analysis (0.61 wt %), which, evaluating the percentage of carbon, hydrogen, nitrogen, and sulfur, also confirms the MABiI molecular formula. The agreement with the calculated values listed in Table 1 is excellent. The chalcogenide has substituted the halide for 1.1% of its amount.

Sulfur inclusion impacted the morphology of the films (Figure 3a,b) with S.MABiI containing elongated grains in addition to the typical hexagonal structures visible in MABiI films and confirming the observation by structural analysis, indicating the existence of multiple crystallite orientations in S.MABiI films compared to a single preferred orientation in MABiI films. Revealing the sulfur presence by EDS was challenging (Figure 3c) due to the low iodine substituted amount (1.1%). A small shoulder where the sulfur signal should be found was the only hint of sulfur because Bi hides the S levels. EDS raw data are displayed in Figure S2 (S.MABiI) and Figure S3 (MABiI).

On the other hand, the sulfur substitution was evident by optical inspection since MABiI films are bright red and S.MABiI films are brown (Figure S4). Since the drop-casted layers are composed of large crystals, transmittance spectra were highly affected by scattered light, so instead of evaluating the optical bandgap from the Tauc plot,[38] we employed the Kubelka–Munk function (Figure 4a),[39] which takes into account only the sample reflectivity. The bandgap is reduced by 0.4 eV upon sulfur doping.[25,26] Photoluminescence (PL) measurements (Figure 4a) were performed and confirmed charge confinement in MABiI: the Stokes shift and the parasitic peaks, typical of cascade excitation, have already been reported with laser sources of 375 and 450 nm.[40] We prove the same effect exciting at 483 nm (Figure 4a), measuring a Stokes shift of 0.5 eV. Also, the parasitic peaks have been observed with energies (0.10 eV) comparable to those reported in the literature (0.13 eV),[40] suggesting photon reabsorption and re-emission. These emissions are typically seen in heavy scintillators.[41−43] The finding should be deeply investigated to be exploited in sensing. S.MABiI, on the other hand, has a negligible Stokes shift, even if the parasitic peaks are still present. The level where recombination happens is probably

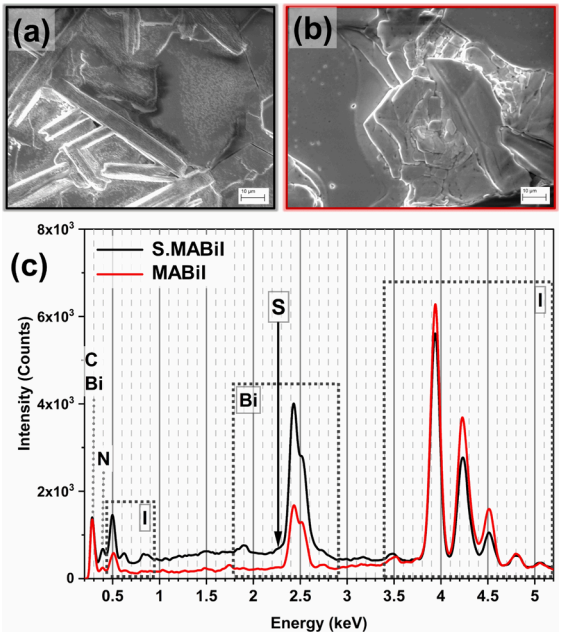

Figure 3. (a) SEM image of a sulfur-doped S.MABiI film. (b) SEM image of an undoped MABiI film. (c) EDS analysis of the sulfur-doped S.MABiI and undoped MABiI layers. Layers were produced by drop-casting on soda-lime glass.

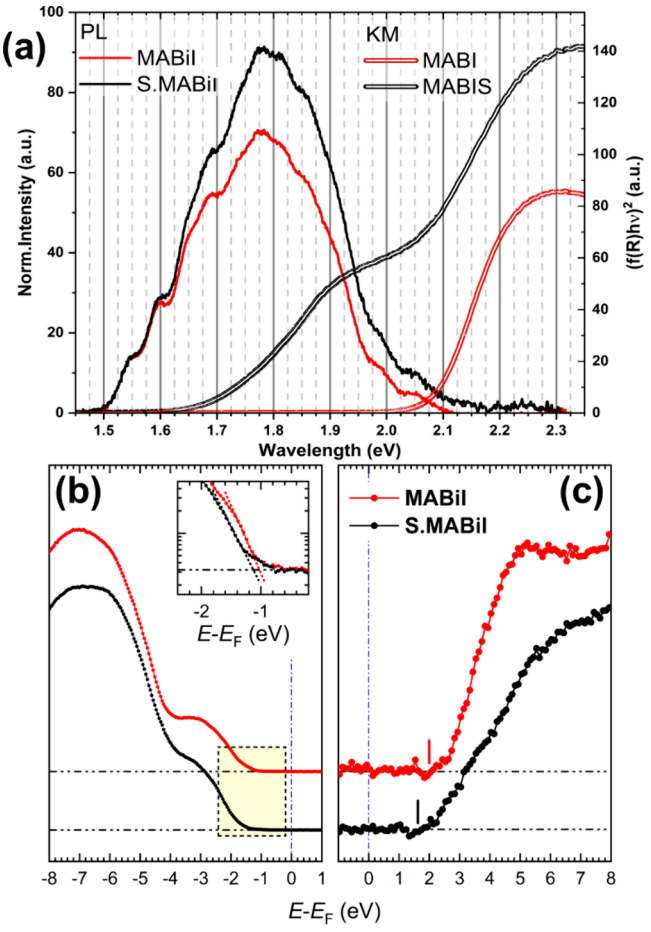

Figure 4. (a) Kubelka–Munk (KM) transformed direct optical transition reflectance spectra for the sulfur-doped S.MABiI and undoped MABiI layers, compared with the photoluminescence (PL) spectra; films are produced by drop-casting on soda-lime glass. (b) UPS and (c) IPES spectra of the sulfur-doped S.MABiI and undoped MABiI layers; films are produced by spin-casting on FTO-coated glass (Spectra are plotted as a function of $E - E_F$, where E_F is the Fermi energy).

https://doi.org/10.1021/acs.jpcc.3c06324
J. Phys. Chem. C 2024, 128, 5408−5417

due to trap states (visible only in emission) most likely located in the $Bi_2I_9^{3-}$ clusters, and both excitons of the pristine and the substituted compounds recombine at the same energy (1.77 eV). Moreover, it has been reported that the excitons at 450 and 375 nm are located in the $Bi_2I_9^{3-}$ clusters with a lifetime in the order of the nanoseconds. It has been suggested that a small portion can tunnel through the $CH_3NH_3^+$ matrix, giving rise to carrier multiplication.[40] Besides, density functional theory has been used to calculate the atomic structures of chalcogenide substituted MABiI, finding out that S substitutes I.[44] Sun et al. also predicted the band gap shrinking, due to the appearance of a significant dispersion at the conduction band bottom.[44] The bottom of the conduction band is mainly composed of the Bi 6p states,[42] which are responsible for the dispersive conduction band edge, while the S 3p states mainly contribute to the valence band.[44]

Therefore, the chalcogenide would not introduce new energy states, since the radiative channel is the same. However, since the lifetimes are long enough to allow delocalization in the matrix, it is reasonable to assume that in S.MABiI the intragap trap levels overlap with the energy levels of the conduction band edge, thus favoring the band-to-band transition. The optical bandgap is dominated by traps, as indicated by the parasitic peaks of the PL, while the electronic bandgap is strongly influenced by the substitution with the chalcogenide, as suggested by the reduction of the Stokes shift.

To know more about the bandgap shrinking, UPS and IPES were performed on 300 nm thin films deposited by spin-coating on a conductive substrate (FTO-coated glass) to minimize sample charging. The UPS and IPES characterization results are shown in Figure 4b,c, respectively, for representative MABiI and S.MABiI samples. Both samples show a similar line shape. The position of the valence and conduction band edges is determined according to the method reported elsewhere.[45,46] The valence band maximum is found at about −1.0 eV relative to the Fermi level for both samples, consistent with the results reported in the literature,[27] while the conduction band minimum is found at about +2.0 and +1.6 eV relative to the Fermi level for MABiI and S.MABiI, respectively, with the conduction band onset shifted by 0.4 ± 0.2 eV toward lower energies for the doped sample. Therefore, the MABiI electronic bandgap is at least 0.7 eV larger than the optical bandgap; i.e., it is heavily influenced by the formation of an optical exciton upon light adsorption[1,40,47] and shows a slight contraction in S-doped samples, consistent with the results of the optical characterization. The data are consistent with the densities of states calculated for S.MABiI.[44] Since the bottom of the conduction band is mainly composed of Bi 6p states, the bismuth interaction with sulfur in S.MABiI broadens the band edge. Thus, the difference between the bandgaps of the two compounds is to be attributed to the structural distortion induced by the substitution of the 1.1% of the halide with the chalcogenide.

Indeed, the sulfur inclusion reduced the electrical resistivity by 2 orders of magnitude: the MABiI film exhibited a resistivity of 2.2 GΩ m and S.MABiI 25 MΩ m (voltage versus current reported in Figure S5). The conductivity enhancement could be ascribed to the energy levels available in the dispersive conduction band edge of S.MABiI,[44] arising thanks to the structure distortion induced by the chalcogenide substitution of two iodine atoms. Therefore, the S inclusion offers new ways for the charge to delocalize, by slightly distorting the structure. The recorded data were corrected for the contact geometry and channel length, since in highly resistive samples, the contact geometry could invalidate the measurement.[48] Accordingly, in the methods suggested by van Reenen and Kemerink,[48] correction factor was estimated to be 1.003. On the other hand, a remarkably high thermal voltage has been recorded. Figure 5a summarizes the data collected on both

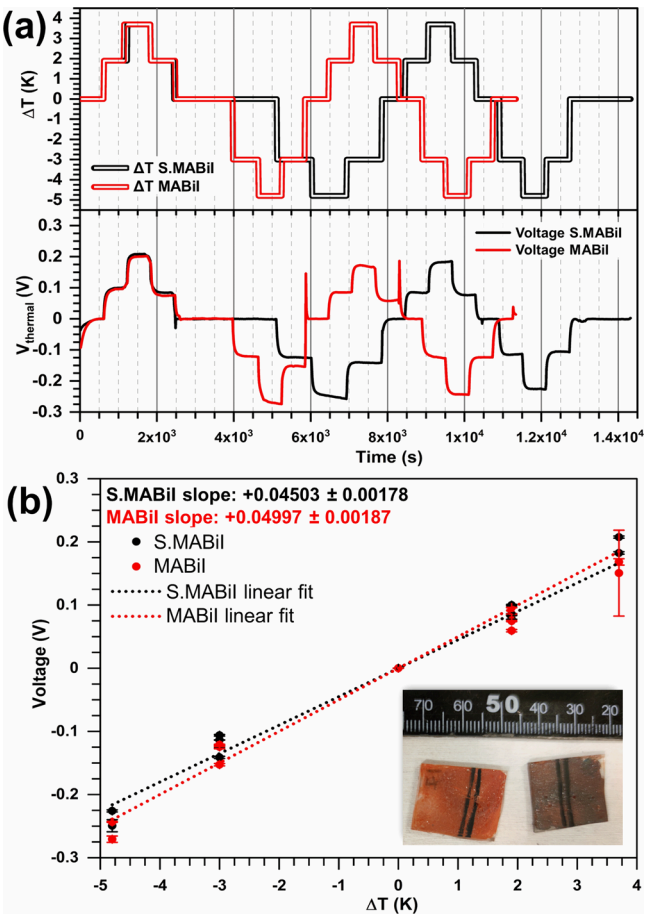

Figure 5. (a) Measured $V_{thermal}$ and temperature difference, ΔT, between two carbon electrodes near 300 K. (b) Linear fitting of $V_{thermal}$ varying ΔT: the linear fit slope gives an uncorrected thermal voltage of 45.03 ± 1.78 mV K^{-1} in S.MABiI and 49.97 ± 1.87 mV K^{-1} in MABiI (inset: samples' picture), which was then corrected to account for the contacts' geometry. In both cases, films were produced by drop-casting on soda-lime glass.

samples, measuring the thermal voltage across some temperature differences, ΔT, near 300 K. The thermal voltage, $V_{thermal}$, (Figure 5b) was measured after the signal was stabilized to be proportional to ΔT. This allowed us to extract thermal voltage of 45.84 ± 1.63 mV K^{-1} in MABiI and 41.31 ± 1.74 mV K^{-1} in S.MABiI near 300 K. The values calculated from the linear fitting in Figure 5b, 49.97 ± 1.87 mV K^{-1} in MABiI and 45.03 ± 1.78 mV K^{-1} in S.MABiI, were corrected, considering the contact geometry and channel length impact on the calculation (samples in Figure 5b, inset).[48] The correction factor was estimated to be 1.09. We applied the same slope method,[49] in the same geometry, on a p-type PEDOT:PSS thin-film (the results presented in Figure S6). The calculated Seebeck coefficient was +14.1 ± 0.4 μV K^{-1} near 300 K, a value in line with the data reported in the literature for PEDOT:PSS processed in a similar way.[50] This thermal voltage cannot be purely a Seebeck voltage as this is generally limited by the

https://doi.org/10.1021/acs.jpcc.3c06324
J. Phys. Chem. C 2024, 128, 5408−5417

relation E_g [eV] = 2e$|S|_{max}$ T_{max}, where E_g is the band gap, T_{max} is the temperature at which the Seebeck coefficient is maximal, and $|S|_{max}$ is the magnitude of the Seebeck coefficient at T_{max}.[51] For a material like MABiI, with $E_g \approx 2$ eV, this places a limit on the magnitude of the Seebeck coefficient of around 3 mV/K. There can be deviations from this relation by a factor of ~2, but it is nonetheless clear that the measured thermal voltage is not entirely thermoelectric. There is most likely a Soret contribution as well since halide perovskites are well-known mixed electron−ion conductors.[52−54]

Despite the large thermal voltage measured in this work and the ultralow thermal conductivity reported elsewhere,[24] the Bi-based perovskite derivates are not ready for a thermoelectric generator technology. Assuming a thermal voltage of 40 mV K^{-1} and thermal conductivity of 0.20 W m^{-1} K^{-1}, the MABiI electrical conductivity should be increased by 9 orders of magnitude to reach a zT of about 1 around room temperature. The challenge is complex, requiring a better understanding of how to increase doping efficiency, but the partial halide substitution with chalcogens could provide one route to reach the ambitious target. Unfortunately, the low solubility of the bismuth precursors prevented control of the doping degree. Besides, it has been reported that ionic compensation of point defects could impact doping efficiency.[16,55] On the other hand, the 40 mV K^{-1} thermal voltage produced by MABiI and S.MABiI can be exploited in thermoelectronics.[49,56−59] Bi-based perovskite derivates are also easily processable, scalable, and cost-effective, and if MABiI and S.MABiI were employed in thermoelectronics, they could allow the device to scale down from millimeters to microns and deliver a thermal voltage higher than that reported in conventional devices.[59−68] Besides, low-dimensional perovskite derivates are increasingly attracting the interest of applied research, thanks to the possibility of exploiting the phenomena resulting from charge confinement in bulk materials.

3. CONCLUSIONS

We have demonstrated a positive thermal voltage exceeding 40 mV K^{-1} in doped and undoped Bi-based perovskite derivates (45.8 mV K^{-1} in MABiI and 41.3 mV K^{-1} in S.MABiI) near 300 K. We also showed that the sulfur substitution effectively reduces the resistivity in MABiI, offering a new path to the confined exciton to tunnel. A computational model to sustain the findings and support the design of a strategy to fine control the substitution amount could further improve the electrical conductivity and, so, the thermopower, opening the way for the implementation of Bi-based perovskite derivates in thermoelectrics. In the meantime, thanks to the easy processability, low-cost production, scalability, and above all, the remarkable thermal voltage delivered per degree Kelvin, the reported compounds could be revolutionary in thermoelectronics. Still, a lot more has to be done to understand the nature of the charge conduction and light emission in quasi-0D perovskites. Before exploitation, understanding and control should be reached. The findings reported here contribute to understanding and aim to stimulate the discussion on how to reach the control.

4. EXPERIMENTAL SECTION

4.1. Materials. The bismuth(III) ethylxanthate, $Bi(xt)_3$, synthesis was carried out following a previously reported method.[25,26] First, bismuth(III) nitrate pentahydrate (Sigma-Aldrich) was dispersed in deionized water to achieve a 0.13 M suspension; then, HCl was slowly added until the solution became clear; finally, a 2 M solution of potassium-*O*-ethyldithiocarbonate (Merck Chemicals) in deionized water was added under moderate stirring. Immediately, a yellow solid precipitated. After 1 h of moderate stirring, the resulting bismuth(III) ethylxanthate, $Bi(xt)_3$, powder was filtered and dried under a vacuum. ^{1}H NMR (Figure S7) and ^{13}C NMR (Figure S8) are reported in the Supporting Information, and they follow the reported literature.[24] ^{1}H NMR (400 MHz, $CDCl_3$) δ 4.70 (q, J = 7.1 Hz, 2H), 1.50 (t, J = 7.1 Hz, 3H). ^{13}C NMR (101 MHz, $CDCl_3$) δ 226.04, 71.43, 13.96. The 1 M precursor solutions were prepared in dimethylformamide, DMF (anhydrous 99.8%, Sigma-Aldrich), by mixing 0.40 M BiI_3 (99%, Sigma-Aldrich) and 0.60 M CH_3NH_3I (99.9%, Ossila) for undoped MABiI synthesis and 0.32 M BiI_3, 0.03 M $Bi(xt)_3$, and 0.57 M CH_3NH_3I for S.MABiI. The entire procedure was carried out in a nitrogen-filled glovebox: the suspensions were left stirring overnight at 70 °C and filtered through a 0.2 μm PVDF filter, and finally, the solutions were stored in dark conditions.

4.2. Samples. Substrates were cleaned in an ultrasonic bath with isopropyl alcohol for 10 min and treated in a UV ozone system (Novascan PSD Pro Series − Digital UV Ozone System) for 30 min. Drop-casted samples were produced in a nitrogen-filled glovebox: 10 μL of precursor solution was dropped on a 1.5 cm × 1.5 cm soda-lime glass substrate and placed on a turned-off hot plate. After 90 s, the temperature raised and stabilized at 75 °C, then at 100 °C, and finally at 125 °C for 15 min for each step. Samples were suddenly cooled down, moving them on a cold surface. As reported in the literature,[69] a high vacuum treatment can remove the unreacted methylammonium at the grain boundaries, so MABiI and S.MABiI samples were left overnight under vacuum (2.0×10^{-6} mBar). The drop-cast MABiI film thickness was 3 μm, and the S.MABiI one was 3.5 μm. Spin-coated samples were produced in a nitrogen-filled glovebox: 20 μL of precursor solution was dropped on a 1 cm × 1 cm fluorine-doped tin oxide (TEC7, Pilkington FTO Glass) coated glass and spun at 3500 rpm (RPM) for 45 s. Soon afterward, the samples were placed on a hot plate at 125 °C and left for 15 min. Samples were then moved to a cold surface and left in a vacuum chamber at 2.0×10^{-6} mBar overnight. The spin-coated MABiI film thickness was 300 nm, and for S.MABiI, it was 320 nm. Electrical contacts were realized by painting a perovskite-grade carbon paste (Dycotec DM-CAP-4701S) with a 00-size paintbrush (Winsor and Newton) and drying at 100 °C on a hot plate. PEDOT:PSS (PH1000 from Heraeus) was spin-coated at 1000 rpm for 1 min on Cr(10 nm)/Au(90 nm) prepatterned glass substrates. The PEDOT:PSS sample was then annealed at 120 °C for 15 min to remove all the residual solvent.

4.3. Characterization. ^{1}H and ^{13}C nuclear magnetic resonance (NMR) spectra were recorded on a Bruker NMR spectrometer, Bruker Avance III 400, at 298 K. Chemical shifts (δ) are reported in parts per million (ppm), using the residual solvent peaks as the internal standard (for ^{1}H NMR (δ): $CDCl_3$ 7.26; for ^{13}C NMR (δ): $CDCl_3$ 77.16).

Sample and contact thicknesses were measured with a VEECO Dektak 8 Stylus Profiler.

The crystallographic structures of MABiI and S.MABiI were observed by X-ray diffraction (XRD) using a Rigaku Miniflex

https://doi.org/10.1021/acs.jpcc.3c06324
J. Phys. Chem. C 2024, 128, 5408−5417

600 system (HyPix-400 MF 2D − HPAD; F.F tube: 15 mA, 40 kV; RS = 0.3 mm, DS/SS = 1.25°).

Raman spectra were recorded by a Jasco Ventuno μ-Raman apparatus equipped with a Peltier-cooled charge-coupled device (CCD) camera (working temperature: −50 °C) and a He−Ne laser (wavelength: 633 nm).

2D-GIWAXS images were collected at the XRD1 beamline of the ELETTRA synchrotron radiation facility in Trieste (Italy). A Pilatus 2 M silicon pixel X-ray detector (DECTRIS Ltd., Baden, Switzerland) was positioned perpendicular to the incident beam 300 mm away from the sample (λ = 1.0 A and beam size of 100 × 100 μm^2). The X-ray beam grazing incident angle was chosen αi = 0.3°, probing the full film thickness. The visualization and analysis of the recorded 2D-GIWAXS images were performed using the open software GIDVis suite of programs.[70]

X-ray photoelectron spectroscopy (XPS) data were collected using a Thermo Scientific Nexsa Surface Analysis System; the reported spectra were recorded using a 1 mm diameter spot after etching with an ions cluster beam (8000 eV; cluster size 1000) three times for 20 s each.

The C, H, N, and S elemental composition in the thin films was determined by using a Vario Micro CHNS Analyzer.

A Jasco V-770 UV−vis/NIR spectrophotometer fitted with a 60 mm UV−visible/NIR integrating sphere (Jasco FLH-740) was used to measure the reflectance in the 300−1300 nm spectral region.

Fluorescence microscopy analyses were performed at θ = 0° on an inverted confocal microscope (ECLIPSE Ti, Nikon); the excitation source was a white Mercury Lamp coupled with a set of colored bandpass filters to select the excitation band wavelengths. In all our experiments, the excitation was selected to be centered at 485 nm, with a 25 nm width band. The emission was cut by a dichroic mirror and a bandpass filter that has a wavelength cutoff at 540 nm. The light was focused on the film and collected by an oil-immersion objective of 100× with a numerical aperture of 1.4. The circular light spot has a diameter of roughly 30 μm. To record the fluorescence spectra, the emitted light was focused on the slit of a Triax monochromator (Horiba Scientific), dispersed by a 150-line grating, and recorded by a cooled CMOS camera.

Ultraviolet photoelectron spectroscopy (UPS) and isochromatic inverse photoemission spectroscopy (IPES) were performed in a custom-made ultrahigh vacuum spectrometer. UV radiation for UPS was provided by a helium discharge lamp (He I line, $h\nu$ = 21.2 eV), and photoelectrons were collected by a 150 mm hemispherical analyzer from Specs GmbH. IPES was performed by sending low-energy electrons on the sample from a GaAs photocathode and detecting 9.6 eV photons.[71] The overall full width at half-maximum resolution of the spectrometer was about 50 (700) meV for UPS (IPES). For these measurements, samples were transferred to the spectrometer in a nitrogen-filled enclosure and swiftly inserted into the vacuum system.

The thermoelectric response and electrical conductivity were measured using a semiconductor parameter analyzer (Keithley 4200-SCS) in a nitrogen-filled glovebox. A Keithley 2230-30-1 (triple channel DC power supply) was used to control the two Peltier plates and apply the temperature gradient to the sample. The applied temperature was evaluated by a thermocouple, waiting for the value to be stable. $I-V$ measurements were performed during the nighttime in a nitrogen-filled glovebox and dark conditions.

Morphology characterization and elemental analysis were performed by Scanning Electron Microscopy/Energy Dispersive Spectroscopy (SEM/EDS; ZEISS Sigma 500) at 15 keV.

Data analysis was performed through different software. XPS surveys were analyzed using the Thermo Avantage v5.9911 software. Raman and the XPS high-resolution core-level data were fitted with Gaussian−Lorentzian cross-product functions using OriginPro 2020. The contact geometry was evaluated using ImageJ. Vesta software has been used to draw the MABiI crystal structure.

■ ASSOCIATED CONTENT

Supporting Information

The Supporting Information is available free of charge at https://pubs.acs.org/doi/10.1021/acs.jpcc.3c06324.

EDS spectra; electrical resistance measurement; measured $V_{thermal}$ and Seebeck coefficient of a PEDOT:PSS thin film; ^{1}H NMR and ^{13}C NMR spectra of the synthesized $(C_2H_5OCS_2)_3Bi$ [Bi(xt)$_3$] powder (PDF)

■ AUTHOR INFORMATION

Corresponding Authors

Vanira Trifiletti − *Department of Materials Science and L-NESS, University of Milano-Bicocca, I-20125 Milan, Italy; School of Engineering and Materials Science, Queen Mary University of London, London E1 4NS, United Kingdom;* orcid.org/0000-0003-4066-3426; Email: vanira.trifiletti@unimib.it

Oliver Fenwick − *School of Engineering and Materials Science, Queen Mary University of London, London E1 4NS, United Kingdom;* orcid.org/0000-0001-7499-5117; Email: o.fenwick@qmul.ac.uk

Authors

Matteo Massetti − *Laboratory of Organic Electronics, Department of Science and Technology, Linköping University, Norrköping SE-601 74, Sweden*

Alberto Calloni − *Dipartimento di Fisica, Politecnico di Milano, 20133 Milano, Italy;* orcid.org/0000-0002-7389-2703

Sally Luong − *School of Engineering and Materials Science, Queen Mary University of London, London E1 4NS, United Kingdom*

Andrea Pianetti − *Department of Materials Science and L-NESS, University of Milano-Bicocca, I-20125 Milan, Italy*

Silvia Milita − *Institute for Microelectronics and Microsystems (CNRIMM), 40129 Bologna, Italy;* orcid.org/0000-0002-9612-2541

Bob C. Schroeder − *Department of Chemistry, University College London, London WC1H 0AJ, United Kingdom;* orcid.org/0000-0002-9793-631X

Gianlorenzo Bussetti − *Dipartimento di Fisica, Politecnico di Milano, 20133 Milano, Italy;* orcid.org/0000-0001-8556-8014

Simona Binetti − *Department of Materials Science and L-NESS, University of Milano-Bicocca, I-20125 Milan, Italy;* orcid.org/0000-0002-8605-3896

Simone Fabiano − *Laboratory of Organic Electronics, Department of Science and Technology, Linköping University, Norrköping SE-601 74, Sweden;* orcid.org/0000-0001-7016-6514

https://doi.org/10.1021/acs.jpcc.3c06324
J. Phys. Chem. C 2024, 128, 5408−5417

Complete contact information is available at:
https://pubs.acs.org/10.1021/acs.jpcc.3c06324

Notes

The authors declare no competing financial interest.

■ ACKNOWLEDGMENTS

V.T. acknowledges the Marie Skłodowska-Curie Action (grant agreement 798271) of the European Union's Horizon 2020 research and innovation program, the Royal Society International Exchanges Award (IESR3193231), and Fondo di Ateneo Quota Competitiva, University of Milan-Bicocca (2023-ATEQC-0078). B.C.S. acknowledges financial support from Innovate UK (Project No. 56338). A.P. and S.B. are grateful to the MUSA – Multilayered Urban Sustainability Action – project, funded by the European Union – NextGenerationEU, under the National Recovery and Resilience Plan (NRRP) Mission 4 Component 2 Investment Line 1.5: Strengthening of research structures and creation of R&D "innovation ecosystems", set up of "territorial leaders in R&D". O.F. acknowledges the Royal Society University Research Fellowship (UF140372 and URF/R/201013). The authors are grateful to L. Duò (Dipartimento di Fisica, Politecnico di Milano) for useful discussions, G. Tseberlidis (Department of Materials Science, University of Milano – Bicocca) for the inspiring suggestions, and F. Maspero (Department of Materials Science, University of Milano – Bicocca) for the technical support.

■ REFERENCES

(1) Trifiletti, V.; Asker, C.; Tseberlidis, G.; Riva, S.; Zhao, K.; Tang, W.; Binetti, S.; Fenwick, O. Quasi-Zero Dimensional Halide Perovskite Derivates: Synthesis, Status, and Opportunity. *Frontiers in Electronics* **2021**, *2* (16), 1.

(2) Breternitz, J.; Schorr, S. What Defines a Perovskite? *Adv. Energy Mater.* **2018**, *8* (34), 1802366.

(3) Akkerman, Q. A.; Manna, L. What Defines a Halide Perovskite? *ACS Energy Lett.* **2020**, *5* (2), 604–610.

(4) Cui, Y.; Yang, L.; Wu, X.; Deng, J.; Zhang, X.; Zhang, J. Recent progress of lead-free bismuth-based perovskite materials for solar cell applications. *Journal of Materials Chemistry C* **2022**, *10* (44), 16629–16656.

(5) Chen, X.; Jia, M.; Xu, W.; Pan, G.; Zhu, J.; Tian, Y.; Wu, D.; Li, X.; Shi, Z. Recent Progress and Challenges of Bismuth-Based Halide Perovskites for Emerging Optoelectronic Applications. *Advanced Optical Materials* **2023**, *11* (3), 2202153.

(6) Ünlü, F.; Deo, M.; Mathur, S.; Kirchartz, T.; Kulkarni, A. Bismuth-based halide perovskite and perovskite-inspired light absorbing materials for photovoltaics. *J. Phys. D: Appl. Phys.* **2022**, *55* (11), 113002.

(7) Trifiletti, V.; Luong, S.; Tseberlidis, G.; Riva, S.; Galindez, E. S. S.; Gillin, W. P.; Binetti, S.; Fenwick, O. Two-Step Synthesis of Bismuth-Based Hybrid Halide Perovskite Thin-Films. *Materials (Basel)* **2021**, *14* (24), 7827.

(8) Artini, C.; Pennelli, G.; Graziosi, P.; Li, Z.; Neophytou, N.; Melis, C.; Colombo, L.; Isotta, E.; Lohani, K.; Scardi, P.; et al. Roadmap on thermoelectricity. *Nanotechnology* **2023**, *34* (29), 292001.

(9) Snyder, G. J.; Snyder, A. H. Figure of merit ZT of a thermoelectric device defined from materials properties. *Energy Environ. Sci.* **2017**, *10* (11), 2280–2283.

(10) Goldsmid, H. J. *Introduction to Thermoelectricity*; Springer: Berlin, Heidelberg, 2016.

(11) Long, X.; Pan, Z.; Zhang, Z.; Urban, J. J.; Wang, H. Solvent-free synthesis of organometallic halides CH3NH3PbI3 and (CH3NH3)-3Bi2I9 and their thermoelectric transport properties. *Appl. Phys. Lett.* **2019**, *115* (7), No. 072104.

(12) Freer, R.; Powell, A. V. Realising the potential of thermoelectric technology: a Roadmap. *Journal of Materials Chemistry C* **2020**, *8* (2), 441–463.

(13) Haque, M. A.; Kee, S.; Villalva, D. R.; Ong, W. L.; Baran, D. Halide Perovskites: Thermal Transport and Prospects for Thermoelectricity. *Adv. Sci. (Weinh)* **2020**, *7* (10), 1903389.

(14) Filippetti, A.; Caddeo, C.; Delugas, P.; Mattoni, A. Appealing Perspectives of Hybrid Lead–Iodide Perovskites as Thermoelectric Materials. *J. Phys. Chem. C* **2016**, *120* (50), 28472–28479.

(15) Lee, W.; Li, H.; Wong, A. B.; Zhang, D.; Lai, M.; Yu, Y.; Kong, Q.; Lin, E.; Urban, J. J.; Grossman, J. C.; Yang, P. Ultralow thermal conductivity in all-inorganic halide perovskites. *Proc. Natl. Acad. Sci. U. S. A.* **2017**, *114* (33), 8693–8697.

(16) Tang, W.; Zhang, J.; Ratnasingham, S.; Liscio, F.; Chen, K.; Liu, T.; Wan, K.; Galindez, E. S.; Bilotti, E.; Reece, M.; et al. Substitutional doping of hybrid organic–inorganic perovskite crystals for thermoelectrics. *Journal of Materials Chemistry A* **2020**, *8* (27), 13594–13599.

(17) He, Y.; Galli, G. Perovskites for Solar Thermoelectric Applications: A First Principle Study of CH3NH3AI3 (A = Pb and Sn). *Chem. Mater.* **2014**, *26* (18), 5394–5400.

(18) Yan, L.; Wang, M.; Zhai, C.; Zhao, L.; Lin, S. Symmetry Breaking Induced Anisotropic Carrier Transport and Remarkable Thermoelectric Performance in Mixed Halide Perovskites CsPb(I(1-x)Br(x))(3). *ACS Appl. Mater. Interfaces* **2020**, *12* (36), 40453–40464.

(19) Jung, Y.-K.; Han, I. T.; Kim, Y. C.; Walsh, A. Prediction of high thermoelectric performance in the low-dimensional metal halide Cs3Cu2I5. *npj Computational Materials* **2021**, *7* (1), 51.

(20) Liu, T.; Zhao, X.; Li, J.; Liu, Z.; Liscio, F.; Milita, S.; Schroeder, B. C.; Fenwick, O. Enhanced control of self-doping in halide perovskites for improved thermoelectric performance. *Nat. Commun.* **2019**, *10* (1), 5750.

(21) Zheng, L.; Zhu, T.; Li, Y.; Wu, H.; Yi, C.; Zhu, J.; Gong, X. Enhanced thermoelectric performance of F4-TCNQ doped FASnI3 thin films. *Journal of Materials Chemistry A* **2020**, *8* (47), 25431–25442.

(22) Nolas, G. S.; Sharp, J.; Goldsmid, J. *Thermoelectrics: Basic Principles and New Materials Developments*; Springer: Berlin, Heidelberg, 2013.

(23) Haeger, T.; Heiderhoff, R.; Riedl, T. Thermal properties of metal-halide perovskites. *Journal of Materials Chemistry C* **2020**, *8* (41), 14289–14311.

(24) Ma, H.; Li, C.; Ma, Y.; Wang, H.; Rouse, Z. W.; Zhang, Z.; Slebodnick, C.; Alatas, A.; Baker, S. P.; Urban, J. J.; Tian, Z. Supercompliant and Soft (CH_3NH_3)_3Bi_2I_9 Crystal with Ultralow Thermal Conductivity. *Phys. Rev. Lett.* **2019**, *123* (15), No. 155901.

(25) Vigneshwaran, M.; Ohta, T.; Iikubo, S.; Kapil, G.; Ripolles, T. S.; Ogomi, Y.; Ma, T.; Pandey, S. S.; Shen, Q.; Toyoda, T.; et al. Facile Synthesis and Characterization of Sulfur Doped Low Bandgap Bismuth Based Perovskites by Soluble Precursor Route. *Chem. Mater.* **2016**, *28* (18), 6436–6440.

(26) Li, J.; Liu, X.; Xu, J.; Chen, J.; Zhao, C.; Salma Maneno, M.; Zhang, B.; Yao, J. Fabrication of Sulfur-Incorporated Bismuth-Based Perovskite Solar Cells via a Vapor-Assisted Solution Process. *Solar RRL* **2019**, *3* (9), 1900218.

(27) Abulikemu, M.; Ould-Chikh, S.; Miao, X.; Alarousu, E.; Murali, B.; Ngongang Ndjawa, G. O.; Barbé, J.; El Labban, A.; Amassian, A.; Del Gobbo, S. Optoelectronic and photovoltaic properties of the air-stable organohalide semiconductor (CH3NH3)3Bi2I9. *Journal of Materials Chemistry A* **2016**, *4* (32), 12504–12515.

(28) Eckhardt, K.; Bon, V.; Getzschmann, J.; Grothe, J.; Wisser, F. M.; Kaskel, S. Crystallographic insights into (CH3NH3)3(Bi2I9): a new lead-free hybrid organic-inorganic material as a potential absorber for photovoltaics. *Chem. Commun. (Camb)* **2016**, *52* (14), 3058–3060.

(29) Lyu, M.; Yun, J.-H.; Cai, M.; Jiao, Y.; Bernhardt, P. V.; Zhang, M.; Wang, Q.; Du, A.; Wang, H.; Liu, G.; Wang, L. Organic−inorganic bismuth (III)-based material: A lead-free, air-stable and solution-processable light-absorber beyond organolead perovskites. *Nano Research* **2016**, *9* (3), 692−702.
(30) Pious, J. K.; Lekshmi, M. L.; Muthu, C.; Rakhi, R. B.; Vijayakumar, C. Zero-Dimensional Methylammonium Bismuth Iodide-Based Lead-Free Perovskite Capacitor. *ACS Omega* **2017**, *2* (9), 5798−5802.
(31) Shah, S.; Bhorde, A.; Hase, Y.; Aher, R.; Doiphode, V.; Waghmare, A.; Punde, A.; Shinde, P.; Rahane, S.; Bade, B. R.; et al. Role of Solvents in the Preparation of Methylammonium Bismuth Iodide (MBI) Perovskite Films for Self-Biased Photodetector Applications. *ACS Appl. Electron. Mater.* **2022**, *4* (6), 2793−2804.
(32) Kamminga, M. E.; de Wijs, G. A.; Havenith, R. W. A.; Blake, G. R.; Palstra, T. T. M. The Role of Connectivity on Electronic Properties of Lead Iodide Perovskite-Derived Compounds. *Inorg. Chem.* **2017**, *56* (14), 8408−8414.
(33) Naphade, R.; Nagane, S.; Shanker, G. S.; Fernandes, R.; Kothari, D.; Zhou, Y.; Padture, N. P.; Ogale, S. Hybrid Perovskite Quantum Nanostructures Synthesized by Electrospray Antisolvent-Solvent Extraction and Intercalation. *ACS Appl. Mater. Interfaces* **2016**, *8* (1), 854−861.
(34) Rajendra Kumar, G.; Dennyson Savariraj, A.; Karthick, S. N.; Selvam, S.; Balamuralitharan, B.; Kim, H. J.; Viswanathan, K. K.; Vijaykumar, M.; Prabakar, K. Phase transition kinetics and surface binding states of methylammonium lead iodide perovskite. *Phys. Chem. Chem. Phys.* **2016**, *18* (10), 7284−7292.
(35) Chen, X.; Myung, Y.; Thind, A.; Gao, Z.; Yin, B.; Shen, M.; Cho, S. B.; Cheng, P.; Sadtler, B.; Mishra, R.; Banerjee, P. Atmospheric pressure chemical vapor deposition of methylammonium bismuth iodide thin films. *Journal of Materials Chemistry A* **2017**, *5* (47), 24728−24739.
(36) Cherusseri, J.; Varma, S. J.; Pradhan, B.; Li, J.; Kumar, J.; Barrios, E.; Amin, M. Z.; Towers, A.; Gesquiere, A.; Thomas, J. Synthesis of air-stable two-dimensional nanoplatelets of Ruddlesden-Popper organic-inorganic hybrid perovskites. *Nanoscale* **2020**, *12* (18), 10072−10081.
(37) Kong, M.; Hu, H.; Wan, L.; Chen, M.; Gan, Y.; Wang, J.; Chen, F.; Dong, B.; Eder, D.; Wang, S. Nontoxic (CH3NH3)3Bi2I9 perovskite solar cells free of hole conductors with an alternative architectural design and a solution-processable approach. *RSC Adv.* **2017**, *7* (56), 35549−35557.
(38) Tauc, J.; Menth, A. States in the gap. *J. Non-Cryst. Solids* **1972**, *8−10* (Supplement C), 569−585.
(39) Alcaraz de la Osa, R.; Iparragirre, I.; Ortiz, D.; Saiz, J. M. The extended Kubelka−Munk theory and its application to spectroscopy. *ChemTexts* **2020**, *6* (1), 2.
(40) Ni, C.; Hedley, G.; Payne, J.; Svrcek, V.; McDonald, C.; Jagadamma, L. K.; Edwards, P.; Martin, R.; Jain, G.; Carolan, D.; et al. Charge carrier localised in zero-dimensional (CH(3)NH(3))(3)-Bi(2)I(9) clusters. *Nat. Commun.* **2017**, *8* (1), 170.
(41) Yang, H.; Peng, F.; Zhang, Q.; Guo, C.; Shi, C.; Liu, W.; Sun, G.; Zhao, Y.; Zhang, D.; Sun, D.; et al. A promising high-density scintillator of GdTaO4 single crystal. *CrystEngComm* **2014**, *16* (12), 2480−2485.
(42) Brunckova, H.; Kolev, H.; Rocha, L. A.; Nassar, E. J.; Moscardini, S. B.; Medvecky, L. XPS characterization and luminescent properties of GdNbO4 and GdTaO4 thin films. *Appl. Surf. Sci.* **2020**, *504*, No. 144358.
(43) Chen, Y.; Zhang, Q.; Wang, X.; Sun, G.; Dou, R.; Zhang, H.; Zhang, J. Structure and luminescence properties of a new heavy scintillator Zr:GdTaO4. *J. Solid State Chem.* **2022**, *311*, No. 123125.
(44) Sun, Y. Y.; Shi, J.; Lian, J.; Gao, W.; Agiorgousis, M. L.; Zhang, P.; Zhang, S. Discovering lead-free perovskite solar materials with a split-anion approach. *Nanoscale* **2016**, *8* (12), 6284−6289.
(45) Schulz, P.; Whittaker-Brooks, L. L.; MacLeod, B. A.; Olson, D. C.; Loo, Y.-L.; Kahn, A. Electronic Level Alignment in Inverted Organometal Perovskite Solar Cells. *Advanced Materials Interfaces* **2015**, *2* (7), 1400532.
(46) Hoye, R. L. Z.; Schulz, P.; Schelhas, L. T.; Holder, A. M.; Stone, K. H.; Perkins, J. D.; Vigil-Fowler, D.; Siol, S.; Scanlon, D. O.; Zakutayev, A.; et al. Perovskite-Inspired Photovoltaic Materials: Toward Best Practices in Materials Characterization and Calculations. *Chem. Mater.* **2017**, *29* (5), 1964−1988.
(47) Scholz, M.; Flender, O.; Oum, K.; Lenzer, T. Pronounced Exciton Dynamics in the Vacancy-Ordered Bismuth Halide Perovskite (CH3NH3)3Bi2I9 Observed by Ultrafast UV−vis−NIR Transient Absorption Spectroscopy. *J. Phys. Chem. C* **2017**, *121* (22), 12110−12116.
(48) Reenen, S. v.; Kemerink, M. Correcting for contact geometry in Seebeck coefficient measurements of thin film devices. *Org. Electron.* **2014**, *15* (10), 2250−2255.
(49) Liu, Y.; Fu, C.; Xie, H.; Zhao, X.; Zhu, T. Reliable measurements of the Seebeck coefficient on a commercial system. *J. Mater. Res.* **2015**, *30* (17), 2670−2677.
(50) Ali, M. Z.; Ishak, K. M. K.; Zawawi, M. A. M.; Jaafar, M.; Ahmad, Z. Simultaneous enhancement of conductivity and Seebeck coefficient of PEDOT:PSS by triflic acid treatment for flexible thermoelectric generator. *Synth. Met.* **2022**, *286*, No. 117037.
(51) Goldsmid, H. J.; Sharp, J. W. Estimation of the thermal band gap of a semiconductor from seebeck measurements. *J. Electron. Mater.* **1999**, *28* (7), 869−872.
(52) Frost, J. M.; Walsh, A. What Is Moving in Hybrid Halide Perovskite Solar Cells? *Acc. Chem. Res.* **2016**, *49* (3), 528−535.
(53) Walsh, A.; Stranks, S. D. Taking Control of Ion Transport in Halide Perovskite Solar Cells. *ACS Energy Lett.* **2018**, *3* (8), 1983−1990.
(54) Zhang, T.; Hu, C.; Yang, S. Ion Migration: A "Double-Edged Sword" for Halide-Perovskite-Based Electronic Devices. *Small Methods* **2020**, *4* (5), 1900552.
(55) Walsh, A.; Scanlon, D. O.; Chen, S.; Gong, X. G.; Wei, S. H. Self-regulation mechanism for charged point defects in hybrid halide perovskites. *Angew. Chem., Int. Ed. Engl.* **2015**, *54* (6), 1791−1794.
(56) Boyer, A.; Cissé, E. Properties of thin film thermoelectric materials: application to sensors using the Seebeck effect. *Materials Science and Engineering: B* **1992**, *13* (2), 103−111.
(57) Zhao, D.; Fabiano, S.; Berggren, M.; Crispin, X. Ionic thermoelectric gating organic transistors. *Nat. Commun.* **2017**, *8*, 14214.
(58) Paolucci, F.; Marchegiani, G.; Strambini, E.; Giazotto, F. Phase-Tunable Thermal Logic: Computation with Heat. *Physical Review Applied* **2018**, *10* (2), No. 024003.
(59) Zhao, D.; Würger, A.; Crispin, X. Ionic thermoelectric materials and devices. *J. Energy Chem.* **2021**, *61*, 88−103.
(60) Brinksmeier, E.; Heinzel, C.; Wilkens, A.; Lang, W.; Seedorf, T. Monitoring of Machining Processes Using Sensor Equipped Tools. *Adv. Eng. Mater.* **2010**, *12* (7), 641−645.
(61) Zhao, D.; Martinelli, A.; Willfahrt, A.; Fischer, T.; Bernin, D.; Khan, Z. U.; Shahi, M.; Brill, J.; Jonsson, M. P.; Fabiano, S.; Crispin, X. Polymer gels with tunable ionic Seebeck coefficient for ultra-sensitive printed thermopiles. *Nat. Commun.* **2019**, *10* (1), 1093.
(62) Lee, Y.; Park, J.; Choe, A.; Cho, S.; Kim, J.; Ko, H. Mimicking Human and Biological Skins for Multifunctional Skin Electronics. *Adv. Funct. Mater.* **2020**, *30* (20), 1904523.
(63) Wu, X.; Gao, N.; Zheng, X.; Tao, X.; He, Y.; Liu, Z.; Wang, Y. Self-Powered and Green Ionic-Type Thermoelectric Paper Chips for Early Fire Alarming. *ACS Appl. Mater. Interfaces* **2020**, *12* (24), 27691−27699.
(64) Reverter, F. A Tutorial on Thermal Sensors in the 200th Anniversary of the Seebeck Effect. *IEEE Sensors Journal* **2021**, *21* (20), 22122−22132.
(65) Hao, Y.; He, X.; Wang, L.; Qin, X.; Chen, G.; Yu, J. Stretchable Thermoelectrics: Strategies, Performances, and Applications. *Adv. Funct. Mater.* **2022**, *32* (13), 2109790.
(66) Chen, B.; Chen, Q.; Xiao, S.; Feng, J.; Zhang, X.; Wang, T. Giant negative thermopower of ionic hydrogel by synergistic

https://doi.org/10.1021/acs.jpcc.3c06324
J. Phys. Chem. C 2024, 128, 5408−5417

coordination and hydration interactions. *Sci. Adv.* **2021**, *7* (48), No. eabi7233.
(67) Chi, C.; An, M.; Qi, X.; Li, Y.; Zhang, R.; Liu, G.; Lin, C.; Huang, H.; Dang, H.; Demir, B.; et al. Selectively tuning ionic thermopower in all-solid-state flexible polymer composites for thermal sensing. *Nat. Commun.* **2022**, *13* (1), 221.
(68) Kim, T. H.; Zhou, Z.; Choi, Y. S.; Costanza, V.; Wang, L.; Bahng, J. H.; Higdon, N. J.; Yun, Y.; Kang, H.; Kim, S.; Daraio, C. Flexible biomimetic block copolymer composite for temperature and long-wave infrared sensing. *Sci. Adv.* **2023**, *9* (6), No. eade0423.
(69) Trifiletti, V.; Manfredi, N.; Listorti, A.; Altamura, D.; Giannini, C.; Colella, S.; Gigli, G.; Rizzo, A. Engineering TiO_2/Perovskite Planar Heterojunction for Hysteresis-Less Solar Cells. *Advanced Materials Interfaces* **2016**, *3* (22), 1600493.
(70) Schrode, B.; Pachmajer, S.; Dohr, M.; Rothel, C.; Domke, J.; Fritz, T.; Resel, R.; Werzer, O. GIDVis: a comprehensive software tool for geometry-independent grazing-incidence X-ray diffraction data analysis and pole-figure calculations. *J. Appl. Crystallogr.* **2019**, *52* (3), 683−689.
(71) Berti, G.; Calloni, A.; Brambilla, A.; Bussetti, G.; Duo, L.; Ciccacci, F. Direct observation of spin-resolved full and empty electron states in ferromagnetic surfaces. *Rev. Sci. Instrum.* **2014**, *85* (7), No. 073901.

https://doi.org/10.1021/acs.jpcc.3c06324
J. Phys. Chem. C 2024, 128, 5408−5417